RSC Advances

PAPER

View Article Online
View Journal | View Issue

Cite this: *RSC Adv.*, 2018, **8**, 27924

A facile strategy for the synthesis of graphene/V_2O_5 nanospheres and graphene/VN nanospheres derived from a single graphene oxide-wrapped VO_x nanosphere precursor for hybrid supercapacitors†

Wei Sun, Xiujie Ji, Guohua Gao* and Guangming Wu*

It remains a challenge to develop a facile approach to prepare positive and negative electrode materials with good electrochemical performance for application in hybrid supercapacitors. In this study, based on a facile strategy, a single graphene oxide-wrapped VO_x nanosphere precursor is transformed into both electrodes through different thermal treatments (*i.e.*, graphene/VN nanospheres negative electrode materials and graphene/V_2O_5 nanospheres positive electrode materials) for hybrid supercapacitors. The conformally wrapped graphene has a significant influence on the electrochemical performance of VN and V_2O_5, deriving from the simultaneous improvements in electronic conductivity, structural stability, and electrolyte transport. Benefitting from these merits, the as-prepared graphene/VN nanospheres and graphene/V_2O_5 nanospheres exhibit excellent electrochemical performance for HSCs with high specific capacitance (83 F g^{-1}) and good long cycle life (90% specific capacitance retained after 7000 cycles). Furthermore, graphene/VN nanospheres//graphene/V_2O_5 nanosphere HSCs can deliver a high energy density of 35.2 W h kg^{-1} at 0.4 kW kg^{-1} and maintain about 70% high energy density even at a high power density of 8 kW kg^{-1}. Such impressive results of the hybrid supercapacitors show great potential in vanadium-based electrode materials for promising applications in high performance energy storage systems.

Received 20th June 2018
Accepted 25th July 2018

DOI: 10.1039/c8ra05298k

rsc.li/rsc-advances

1. Introduction

The rapid development of electronic devices and electric vehicles greatly increases the demand for energy storage devices with high energy density, low cost, and reliable stability.[1,2] As the current main energy power sources, supercapacitors (SCs) have received tremendous attention because of their fast charge/discharge ability, high power density, and notable cycle life. Unfortunately, the practical applications of SCs still remain a stumbling block since their energy densities are far from high-energy-density devices.[3–5] Therefore, the improvement of SCs with high performance and facile methods is highly desirable.

To meet the future energy market, researchers propose hybrid supercapacitors (HSCs),[6–9] which extend the operating voltage through full use of the absolutely opposite potential window of the negative and positive electrode materials.[10,11] It is expected that this hybrid system exhibits reliable cycling stability and battery-like high energy density. In light of the total operating voltage and capacitance governed by positive and negative electrodes, the characteristic of two electrode materials (such as specific capacitance and potential window) are considered as the key component in increasing the energy density of HSCs by maximizing the operating voltage in the systems.[12] Accordingly, considerable research has been focused on fabricating high-performance negative and positive electrode materials. Up to now, various materials, such as transition metal oxides/hydroxides, phosphides or sulfides, have been developed as positive electrode materials in HSCs due to their rich oxidation states and high theoretical-specific capacitance derived from reversible and rapid redox reactions. Thus, extensive research interest has been invested in them. However, the advancement obtained by negative electrode materials is far lagging behind positive electrode materials, which restricts the process of high-performance HSCs. Nowadays, the most widely available negative electrode materials are mainly based on carbonaceous materials, which delivers much lower (3–4 times) specific capacitance (100–250 F g^{-1}) than that of positive electrode materials. Compared with carbonaceous negative electrode materials that based on electrical double layer energy-storage mechanism, pseudocapacitive materials employed as negative electrode materials are becoming one of most promising alternatives for HSCs because they possess higher specific capacitance and energy density. Since the first introduction, few types of pseudocapacitive negative electrode materials have been reported, such as TiO_2,[13] MoO_3,[14] Fe_2O_3,[15,16] and V_6O_{13}.[17]

Shanghai Key Laboratory of Special Artificial Microstructure Materials and Technology, School of Physics and Science Engineering, Tongji University, Shanghai, 200092, PR China. E-mail: gao@tongji.edu.cn; wugm@tongji.edu.cn

† Electronic supplementary information (ESI) available. See DOI: 10.1039/c8ra05298k

For example, Fe_2O_3, used to be the most prominent negative material, exhibits high theoretical-specific capacitance, non-toxicity, and low cost.[18] Raut *et al.* have decorated α-Fe_2O_3 on MWCNT in order to increase their electrical conductivity, which exhibited much higher specific capacitance (431 F g^{-1}) than those of the pristine α-Fe_2O_3 (187 F g^{-1}) and MWCNT (81 F g^{-1}).[19] Despite these efforts, these above mentioned pseudocapacitive negative electrode materials still have relatively limited specific capacitance and power capability. Among these reasons for this, the intrinsically poor electrical conductivity of these electrode materials poses a great influence that confines their electrochemical performance.

In recent years, vanadium nitride (VN) holds considerable promise as negative electrode materials for HSCs because of its versatile merits including high theoretical-specific capacitance (1340 F g^{-1}) and outstanding electrical conductivity (1.67×10^4 Ω^{-1} cm^{-1}) compared with its corresponding oxides.[20–22] Furthermore, VN has high hydrogen evolution potential in aqueous solution, which can deliver a wide working window in negative potential for HSCs.[23] Unfortunately, the morphology of pristine VN commonly consists of accumulational nanoparticles with weak interconnection, which affect the electronic conductivity and restrict the ionic conductivity. As a consequence, its rate capability is degraded greatly. Furthermore, the irreversible oxidation reaction of VN materials causes pulverization and deterioration of their structures during repeated charge/discharge process, leading to poor electrochemical stability.[24,25] For example, the nanocrystalline VN covered on MCNT composite as negative electrode materials showed a specific capacitance of 289 F g^{-1} only with 64% capacitance retention after 600 cycles.[26] The reported strategy to circumvent this stumbling block is to directly coat carbon material on nanoscale VN as protective layer. For example, recently, Zhang *et al.* reported that well-aligned VN nanowire arrays (NWAs) shelled with a carbon layer had a reversible specific capacitance of 715 mF cm^2 and a capacitance retention rate of 90% after 6000 cycles.[27] Despite much progress has been achieved, the trouble of unsatisfied electrochemical performance still exist, probably because of the individual outer carbon coating which cannot fully ensure a fast electron transfer across the whole interfaces of electrode materials. Hence, an upgraded strategy for constructing interconnected conductive network by combing VN nanosphere and carbon network consisting of two-dimensional (2D) graphene (GR) is proposed for high-performance HSCs. Compared to the abovementioned amorphous carbon layer, GR, as 2D structure of carbon atoms, has unique electrical conductivity, large specific surface and structural flexibility, which drives researchers to design composite materials with it for energy storage.

Herein, we have successfully fabricated a graphene oxide (GO)-wrapped VO_x nanosphere (GO-wrapped VO_x NSP) precursor; the uniform VO_x nanospheres are evenly distributed into the GR matrix, interconnecting to form a conductive network structure. Then, through different thermal treatments the precursor can be facilely transformed to GR/VN nanosphere and GR/V_2O_5 nanosphere composites, suitable for the negative and positive electrode materials of HSCs, respectively. As a proof of upgraded strategy, HSCs is assembled based on the single GR-wrapped VO_x nanosphere precursor-derived positive and negative, and excellent electrochemical performance, such as high energy density and enhanced cycle stability, is achieved. This strategy may open up a promising way to new-type supercapacitors with excellent electrochemical performance.

2. Experimental section

2.1 Preparation of GO-wrapped VO_x nanosphere composite

The GO-wrapped VO_x NSP was prepared by following the process previously reported with modifications.[28] Vanadium oxide (VO_x) sol was used as vanadium source, as previously reported by our group.[29] The obtained GO nanosheets were dispersed into ethylene glycol to form suspension with the concentration of 2 mg mL^{-1}, and then ultrasonicated for 30 min. In a typical procedure, 5 mL 3 mg mL^{-1} GO dispersion was firstly mixed uniformly with 5 μL ethylenediamine (EDA) by ultrasonic dispersion for 15 min to give solution A. 16 g commercial V_2O_5 powder was suspended in a 300 mL mixed solution of benzyl alcohol and isopropanol ($C_7H_8O : C_3H_8O = 1 : 7.5$ v/v) under magnetic stirring for 30 min. Then the suspension was heated at 110 °C under condensate reflux for 4 h. After filtration, the filtrate was concentrated to 1/3 volume through heating reflux to given solution B (VO_x sol). 5 mL solution A and 3 mL solution B were poured slowly into a beaker pre-filled with 30 mL isopropyl alcohol and 0.5 mL acetic acid. The solution was stirred for 30 min and then poured into a Teflon-lined autoclave. The autoclave was sealed and maintained at 180 °C for 20 h. After cooling to room temperature, the graphene-wrapped VO_x nanosphere composite was obtained after washing with water and vacuum drying overnight. For comparison, the pure VO_x microspheres were also prepared following the above-mentioned experimental without GO dispersion.

2.2 Preparation of GR/V_2O_5 nanosphere composite

The GO-wrapped VO_x NSP was firstly annealed in N_2 at 300 °C for 1 h with a ramp rate of 1 °C min^{-1}, the temperature was then rose to 350 °C, after which the samples were further annealed in air at 350 °C for 2 h. The obtained was noted as GR/V_2O_5 NSP.

2.3 Preparation of GR/VN nanosphere composite

The GO-wrapped VO_x NSP was directly annealed in NH_3 at 600 °C for 2 h with a ramp rate of 5 °C min^{-1}. The obtained was noted as GR/VN NSP.

2.4 Characterization

Samples were characterized using SEM (XL30FEG), TEM (JEOL-2100 TEM operating at 200 kV), and rotation anode X-ray powder diffraction (XRD) (Rigaku D/max-C) equipped with Cu Kα radiation source (λ = 1.5406 Å). All the electrochemical measurements were conducted using an electrochemical workstation (CHI 660D). The electrochemical studies of the individual electrode were performed in a three-electrode cell, with Pt counter electrode and an Ag/AgCl reference electrode in 8 M LiCl aqueous solution.

2.5 Electrode preparation and electrochemical measurements

The working electrodes were prepared by coating the slurry of the active material, conductive carbon black, and polymer binder (polyvinylidenefluoride, PVDF) with a mass ratio of 90 : 5: 5 using *N*-methylpyrrolidone (NMP) as the solvent on graphite substrates. The electrodes were dried at 120 °C for 12 h under vacuum and the active material loading was about 2 mg cm^{-2}. According the thermogravimetric (TG) analysis (Fig. S2, ESI†), the content of graphene in the final electrode is about 43.3% (the detailed calculations are given in the ESI†). Electrochemical measurements on the capacitive performance are conducted with a CHI 660D electrochemical workstation in an aqueous LiCI electrolyte (8.0 M) using a three-electrode cell, where a Pt foil serves as the counter electrode and a Ag/AgCI as the reference electrode. The specific capacitance was calculated from the galvanostatic discharge curves based on the following equation: $C = I\Delta t/m\Delta V$, where I is the discharge current, Δt is the discharge time, ΔV is the voltage range, and m is the mass of the active material.

The evaluation of HSCs was conducted in a two-electrode cell at room temperature in 8 M LiCI aqueous electrolyte solution. HSCs were fabricated by assembling GR/V_2O_5 NSP cathode and GR/VN NSP anode and the working electrodes were prepared by the above-stated method. The loading mass ratio of active material (GR/V_2O_5 NSP : GR/VN NSP) was estimated according to the well-known charge balance equation ($q_+ = q_-$). In order to get $q_+ = q_-$ at current density of 1 A g^{-1}, the mass ratio was calculated based on the following equation: $\frac{m_{\text{positive}}}{m_{\text{negative}}} = \frac{V_{\text{negative}} \times C_{\text{negative}}}{V_{\text{positive}} \times C_{\text{positive}}}$. The charge stored by each electrode depends on the specific capacitance (C), the voltage range for the charge/discharge process (ΔV) and the mass of the electrode (m). The calculated value of mass ratio between GR/V_2O_5 NSP and GR/VN NSP is about 0.8. The electrode of GR/V_2O_5 NSP and GR/VN NSP contained about 2.3 mg and 3 mg of active materials, respectively, which is close to the optimal mass ratio of 0.8. The two identical electrodes were placed together and separated by a porous nonwoven cloth separator. The energy density (E) and power density (P) of HSCs against the two electrodes in the device are calculated based on the total mass of the active materials using the following equations: $E = 1/2CV^2$ and $P = E/\Delta t$, where V is the potential change during the discharge process and Δt is the discharge time.

3. Results and discussion

3.1 Structural formation mechanism

Raman and infrared spectroscopy were used to confirm the qualities of as-prepared GO and graphene (GR). As shown in Fig. S1a (ESI†), the following functional groups were identified in the sample: O–H stretching vibrations (3420 cm^{-1}), C=O stretching vibration (1726 cm^{-1}), C=C from unoxidized sp^2 CC bonds (1623 cm^{-1}), and C–O vibrations (1060 cm^{-1}).[30] The result of the FTIR spectra confirms the presence of oxygen-containing groups on as-prepared GO surface, which are benefit for forming stable and uniform dispersion. In the Raman spectra (Fig. S1b, ESI†) of as-prepared GO, the G band is prominent and shifted to 1596 cm^{-1}. Meanwhile, the D band at 1355 cm^{-1} becomes dominant, indicating the reduction in size of the in-plane sp^2 domains, due to the extensive oxidation. Comparing with GO, the Raman spectra of GR also contains both D and G bands (at 1348 and 1586 cm^{-1}, respectively) with an increase D/G intensity ratio. This difference implies a decrease in the average size of the sp^2 domains upon reduction of the exfoliated GO.[31] The formation procedure of the GO-wrapped VO_x involves three major steps as schematically displayed in Fig. 1 (see the Experimental section for details). First, the VO_x sol was added to the precursor solution under vigorous stirring to homogenously form the VO_x oligomers by the olation.[32] Due to a strong coordination interaction between the vanadium ions from the VO_x oligomers and oxygen groups from graphene oxide (GO), the oligomers could be easily attached to the surface of GO (stage I). Second, the VO_x nucleuses are generated in the isopropyl alcohol due to the supersaturated formation of VO_x oligomers under high pressure condition of solvothermal reactions (stage II). Simultaneously, the suspended nucleuses in the solution undergo the aggregation process and transform to nanospheres to reduce overall surface free energy in stage III. After the *in situ* solvothermal process, GO-wrapped VO_x NSP was obtained. Then, through different thermal treatment processes, the GO-wrapped VO_x NSP precursor can be either transformed to GR/VN NSP or oxidized to GR/V_2O_5 NSP. Finally, the HSCs device is assembled by using the GR/VN NSP and the GR/V_2O_5 NSP as anode and cathode, respectively.

3.2 Morphology and structure characterization

Fig. 2a and b demonstrate the morphology of the obtained GO-wrapped VO_x NSP as starting material. As shown in the low-magnification SEM (Fig. 2 a), VO_x nanospheres are incorporated into the GO matrix and uniformly wrapped by highly crumpled GO. Meanwhile, these highly crumpled GO sheets constitute a continuous porous network structure (Fig. 2a), which may be beneficial to the rapid transport of electrolyte and the structural stability. The close observation in Fig. 2b reveals that the highly uniform VO_x nanospheres have an average diameter of ~700 nm without obvious particle aggregation. Through different thermal treatments GO-wrapped VO_x NSP can then easily be transformed to vanadium nitride and vanadium oxide. In Fig. 2c and e, it is seen that GR/VN NSP and GR/V_2O_5 NSP is obtained by thermal treatment in ammonia and air, respectively. VN and V_2O_5 nanospheres remain spherical in shape with high uniformity and the crumpled GR uniformly wrapping VN or V_2O_5 nanospheres can be easily found as expected (Fig. 2c and e). No obvious changes can be detected after thermal treating, indicating that the ammonia reduction and air oxidation did not destroy the overall shape and sizes of the GO-wrapped VO_x precursor. Fig. S3a and b (ESI†) show the SEM images of VN and V_2O_5 nanospheres fabricated without GO-ethyleneglycol dispersion in the solvothermal system. Interestingly, compared with GR/VN NSP or GR/V_2O_5 NSP (Fig. 2c and

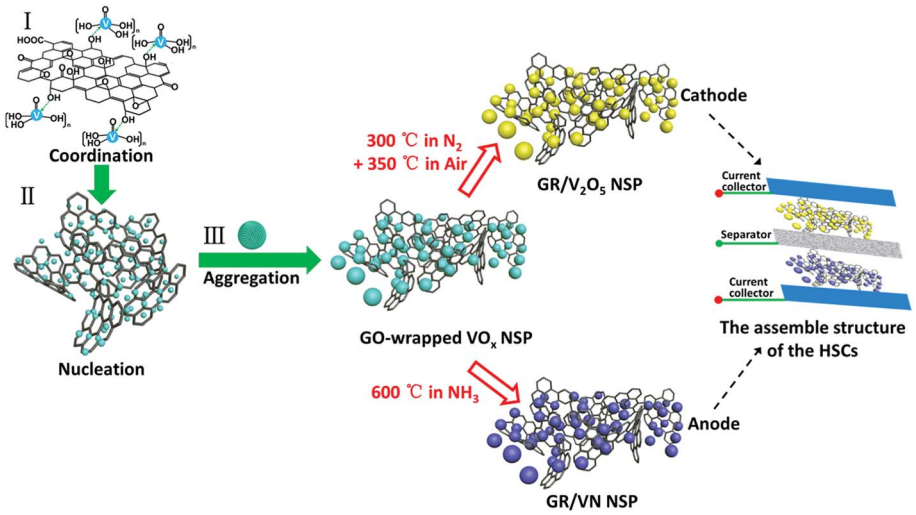

Fig. 1 Schematic illustration of the fabrication process. GR/V_2O_5 NSP cathode and GR/VN anode are obtained from the same GO-wrapped VO_x NSP and assemble into the hybrid supercapacitor.

e), both pristine VN and V_2O_5 nanospheres show larger diameter (~800 nm), implying the GO in solvothermal system as a barrier can restrain the growth of nanospheres. The corresponding EDS spectra in Fig. 2d indicate that the nanospheres are mainly composed of V, N and C elements, suggesting VN have successfully been fabricated. To further confirm the structure of as-prepared samples, STEM-EDS element mapping is performed. As shown in the insets of Fig. 2d and f, uniform distribution of V, N, and O form a sphere morphology, which are in accordance with the mapping area of VN and V_2O_5 nanospheres, respectively. In addition, the C signal area can be detected in both samples, revealing the sophisticated combination of the fabricated GR and vanadium-based nanospheres.

The TEM and high-resolution TEM (HRTEM) were also performed to further analyze the detailed structures of the samples. The TEM images in Fig. 3a and d manifest the VN nanospheres and V_2O_5 nanospheres remain spherical in shape with diameter of ~600 nm. In comparison with the spheres before the thermal treatment, a slight contraction of spheres is detected, resulting from the thermal annealing process. Meanwhile, the visible GR can be easily found and the nanospheres are extreme evenly wrapped by highly crumpled GR in the nanostructure of both samples, which is consistent with the SEM results. The HRTEM image taken from the corresponding nanosphere in Fig. 3b depicts that VN nanosphere has a clear crystalline structure with the lattice spacing of 0.24 and 0.21 nm, which are in good agreement with d-spacing of (111) and (200) plane of cubic VN (JCPDS Card no. 35-0768). As for GR/V_2O_5 NSP, Fig. 3e suggests the inter-planar spacing is about 0.26 and 0.34 nm which corresponds to the (310) and (110) plane of the orthorhombic phase V_2O_5 (JCPDS, Card no. 41-1426). The corresponding selected area electron diffraction (SAED) patterns of GR/VN NSP and GR/V_2O_5 NSP in the top-right insets of Fig. 3b and e imply the excellent crystallinity of the obtained samples by the thermal annealing process. The X-ray diffraction (XRD) patterns of the ammonia thermal treatment and the air thermal treatment are shown in Fig. 3c and f, the peaks from ammonia treatment product could be assigned to (111), (200), (220) and (222) lattice planes of cubic VN, respectively and the peaks obtained from the air treatment product could be indexed to (200), (001), (101) and (110) diffraction of orthorhombic V_2O_5. No obvious peaks from other phases can be observed in both samples, demonstrating the obtained materials with high purity and the complete conversion from GO-wrapped VO_x NSP during the thermal treatment.

3.3 Electrochemical performance of GR/VN NSP and GR/V_2O_5 NSP

GR/VN NSP negative material. To explore the electrochemical behavior, cyclic voltammetry (CV), galvanostatic charge/discharge (GCD), and electrochemical impedance spectroscopy (EIS) of as-formed GR/VN NSP were investigated employing a three-electrode system using 8 M LiCI aqueous solution. Fig. 4a presents the cyclic voltammogram (CV) curves for GR/VN NSP in a potential window between −1.2 and 0 V at different sweep rates. It should be noted that two broad redox humps and the wide current potential response appeared for GR/VN NSP in all CV curves, implying that the capacitance characteristics of the sample are composed of redox pseudocapacitance and electrical double layer capacitance.[33] The anodic and cathodic peaks display symmetric geometry as the sweep rate from 10 to 100 mV s^{-1}, suggesting the excellent reversibility of GR/VN NSP electrode.[34] From the plots of log(current density) *versus* log(sweep rate) from the 5 to 100 mV s^{-1} for both cathodic and anodic peaks (Fig. 4b), the current follows well a power-law relationship with the sweep rate ($I_p = av^b$).[35] Whereas a *b*-value of 0.5 would indicates that the current is controlled by diffusion-controlled process, while a value close to 1 indicates that the current is surface-controlled.[36,37] Clearly, it can be concluded that the electrode kinetics under the conditions investigated is majorly surface-controlled, and hence is fast, which indicates the better kinetics can be obtained with

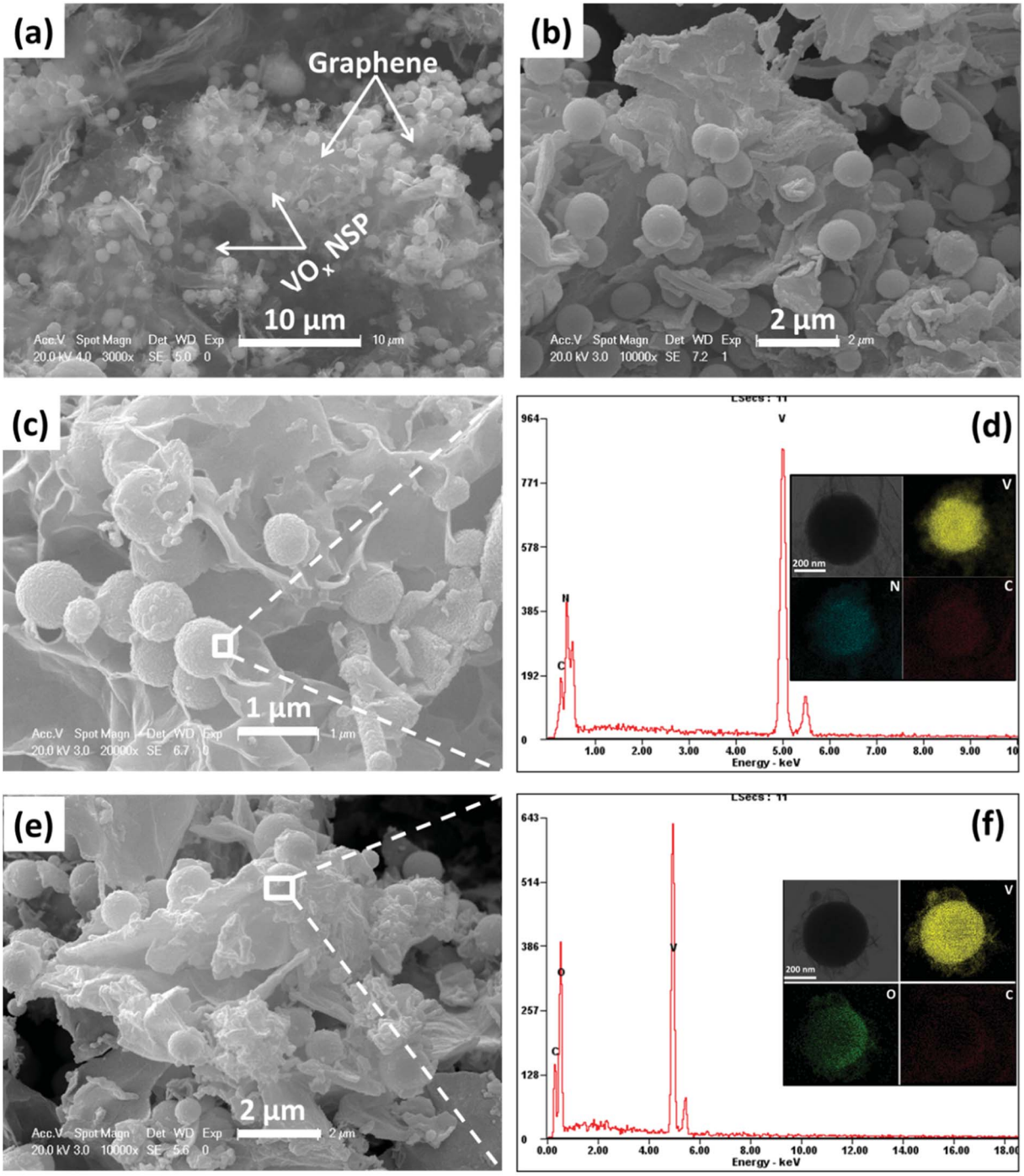

Fig. 2 SEM images of the as-prepared samples. (a and b) GO-wrapped VO_x NSP, (c) GR/VN NSP, and (e) GR/V_2O_5 NSP. (d) and (f) show EDS spectrum of GR/VN NSP and GR/V_2O_5 NSP, respectively. Inset of (d) and (f): STEM, and STEM-EDS element mapping images of the corresponding samples.

the existence of GR. The GCD curves of GR/VN NSP are shown in Fig. 4c. All the curves are nearly linear and show a symmetrical distribution, which confirms perfect reversibility of the pseudocapacitive reactions for the sample. The GR/VN NSP delivers an impressive specific capacitance of 375 F g^{-1} at current density of 0.5 A g^{-1} (Fig. 4c), which is obviously higher than that of conventional carbon-based negative electrodes,[38–40] as well as most VN-based electrodes.[20,24,41] Furthermore, the GR/VN NSP electrode exhibits an excellent rate capability, with a retention rate of 73% when the current density increases from 1 to 10 A g^{-1}, which is higher than that of nanocrystalline VN nanostructures.[20,42] The high electrochemical performance of GR/VN NSP can be attributed to the porous network structure, enabling effective electrolyte transport and active-site accessibility, and the highly conductive GR, facilitating faster electron transports. The cycling stability is critical for VN-based

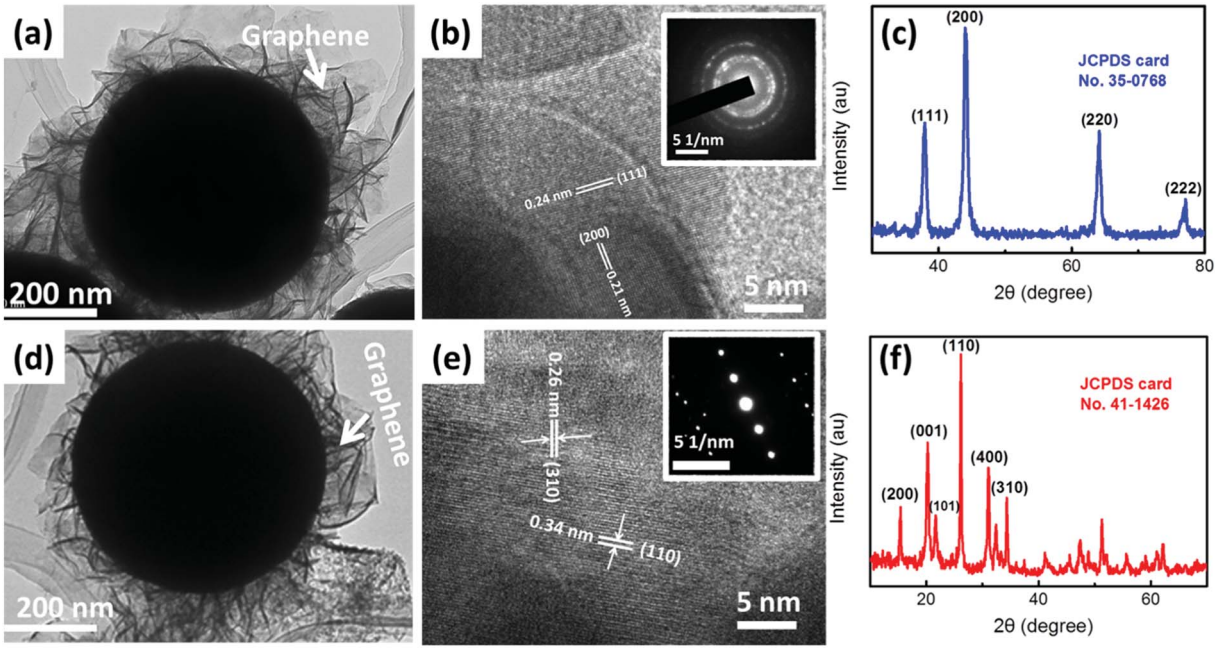

Fig. 3 TEM images of the as-prepared sample. (a) GR/VN NSP and (d) GR/V_2O_5 NSP. High-resolution (HRTEM) images of (b) GR/VN NSP and (e) GR/V_2O_5 NSP, inset image is the corresponding selected area electron diffraction (SAED) patterns of samples. XRD patterns: (c) GR/VN NSP and (f) GR/V_2O_5 NSP.

electrode materials, because that the irreversible oxidation reaction seriously restricted its further applications in higher performance HSCs. As shown in Fig. S4 (ESI†), compared with the pure VN nanospheres, the GR/VN NSP endow long-term cycling stability, which may be due to the highly crumpled GR wrapping on the surface of VN nanospheres suppresses electrochemical oxidation and dissolution of the inner VN. Thus,

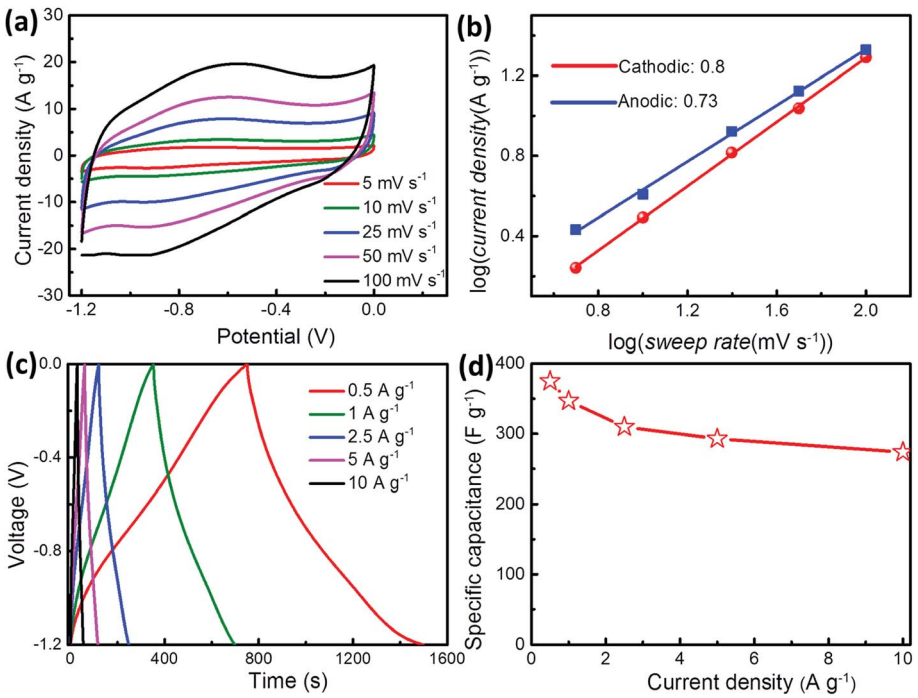

Fig. 4 Electrochemical characteristic of GR/VN NSP in a three-electrode system. (a) CV curves at different sweep rates. (b) The dependence of the peak current density on square root of weep rate. (c) Galvanostatic charge–discharge curves at the different current density. (d) Specific capacitance of the sample as a function of current density.

the as-prepared GR/VN NSP is a most promising candidate electrode material for HSCs.

Similarly, the electrochemical properties of as-formed GR/V_2O_5 NSP were also evaluated using CV curves and the galvanostatic test. Representative CV curves of V_2O_5-based electrode material at sweep rates ranging from 5 to 100 mV s^{-1} in the potential range of −0.3–0.7 V are shown in Fig. 5a. Apparently, the redox peaks are visible in CV curves, indicating the capacitance of GR/V_2O_5 NSP is mainly dominated by the redox mechanism. In addition, it can be seen clearly from Fig. 5a that the redox peaks of each CV curve keep explicit and symmetric as the sweep rates increase from 5 to 100 mV s^{-1}, suggesting the perfect electrochemical reversibility.[43] As shown in Fig. 5b, the GCD curves at various current densities exhibit symmetrical distribution, implying the high coulombic efficiency for the sample during consecutive charge/discharge process. Utilizing the discharge curves, the specific capacitance of GR/V_2O_5 NSP electrode as a function of current density is 580, 517, 453.3, 378, and 327.5 F g^{-1}, at current densities of 0.5, 1, 2.5, 5, and 10 A g^{-1}, respectively (Fig. 5c). Notably, with the augment of current density up to 10 A g^{-1}, GR/V_2O_5 NSP electrode can still deliver a high capacitance retention (56%), compared with 35% (180 F g^{-1}) for the pure V_2O_5 NSP (Fig. 5c), which sufficiently proves the superior rate capability of GR/V_2O_5 NSP. The enhanced electrochemical performance of GR/V_2O_5 NSP may be attributed to the interconnected electrical conductive network consisting of GR and synergistic effect between GR and V_2O_5 nanospheres. The EIS tests were carried out to further understand their capacitive behaviors. As shown in Fig. 5d, differing from the pure V_2O_5 nanospheres, the semicircle in high-frequency range is very small and the deviation in the slope of the line in low-frequency range is close to the 90° phase angle, manifesting the good conductivity and excellent operation rate of the GR/V_2O_5 NSP as the electrode material. Inset of Fig. 5d is the magnified area of the high frequency portion, from which the charge transfer resistance (R_{ct}) of the pure V_2O_5 NSP electrode can be obtained as 1.8 Ω, whereas that of the composite material electrode is only 1.1 Ω, which further confirms its good electrochemical performance. Both GR/VN NSP and GR/V_2O_5 NSP composite electrode materials exhibit the good electrochemical performance, especially high specific capacitances. This is mainly attributed to the combination of redox capacitance from pseudocapacitive species (V_2O_5 and VN) and electric double layer capacitance (EDLC) from graphene in the composite electrode materials. Furthermore, the porous network constructed by graphene nanosheets also expedites efficient charge transport for V_2O_5 and VN.

3.4 Hybrid supercapacitor based on GR/VN NSP and GR/V_2O_5 NSP

The hybrid supercapacitor using the GR/V_2O_5 NSP and GR/VN NSP as the positive electrode and negative electrode, respectively, was assembled as shown in Fig. 1 to further evaluate the practical application of the two samples. To assess the best total voltage of HSCs, CV curves were used to evaluate the applicable operation voltage window (OVW) at low sweep rate of 5 mV s^{-1}, as shown in Fig. 6a. Utilizing the complementary potential windows ranges of GR/VN NSP and GR/V_2O_5 NSP (Fig. 6a), it is anticipated that the OVW for the assemble HSCs can reach 1.9 V. But in CV testing process, the obvious polarization derived from oxygen evolution reactions is occurring in Fig. 6b

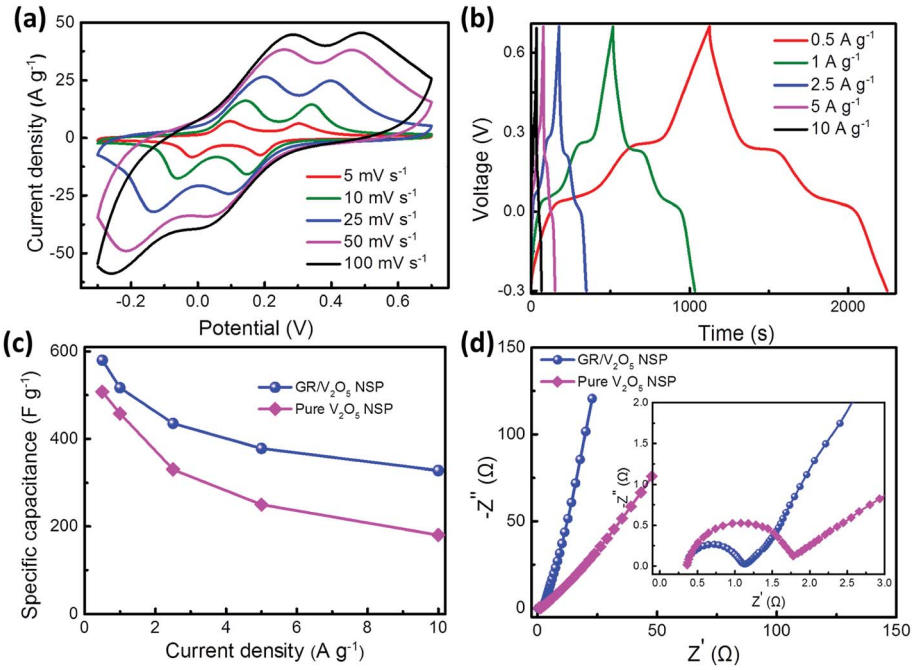

Fig. 5 Electrochemical characteristic of GR/V_2O_5 NSP in a three-electrode system. (a) CV curves at different sweep rates. (b) Galvanostatic charge–discharge curves at the different current density. (c) Specific capacitance of the sample as a function of current density. (d) Nyquist plots of experimental impedance.

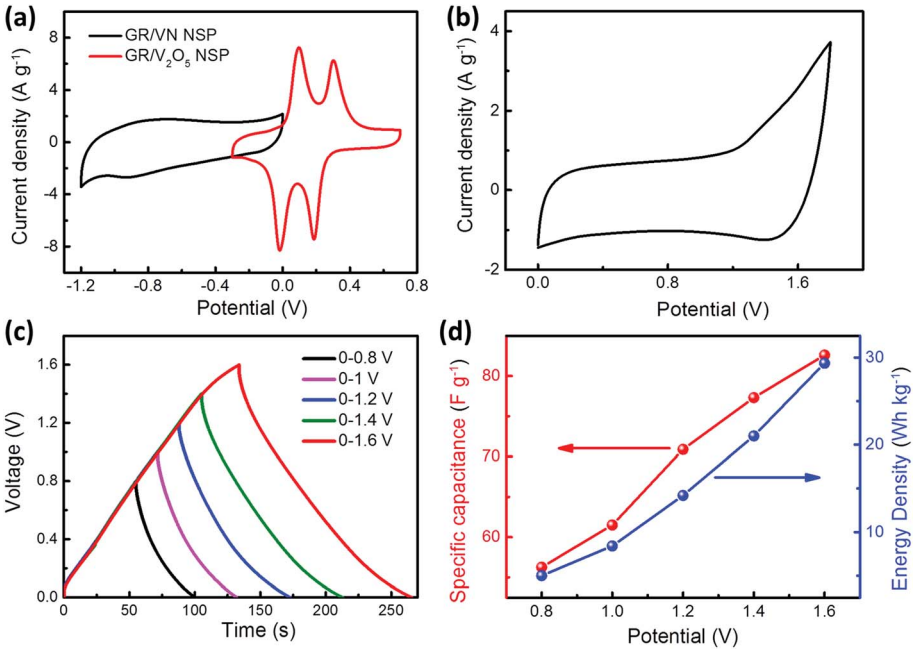

Fig. 6 Electrochemical characterization of HSCs. (a) CV obtained for GR/VN NSP and GR/V_2O_5 NSP at a sweep rate of 5 mV s^{-1} in a three-electrode system. (b) CV curves of HSCs measured at operating voltages over 1.6 V at a constant sweep rate of 15 mV s^{-1}. (c) Galvanostatic charge–discharge curves of the HSCs device collected over different voltages from 0.8 to 1.6 V at a current density of 1 A g^{-1}. (d) Specific capacitance and energy density calculated based on galvanostatic charge–discharge curves obtained at 1 A g^{-1} as a function of the potential window.

when the OVW is over 1.7 V. Thus, the maximum OVW for the HSCs based on GR/VN NSP and GR/V_2O_5 NSP should be 0–1.6 V. Fig. S5 (ESI†) shows the CV profiles of the GR/VN NSP//GR/V_2O_5 NSP HSCs at a sweep rate of 15 mV s^{-1} in different potential windows. When OVW is located at 1 V, a triangular CV curve implies an incomplete pseudocapacitive response from the HSCs. By increasing the OVW to 1.2 V, a pair of redox humps appears in the CV curves, showing the pseudocapacitive properties. Furthermore, at a high potential window up to 1.6 V, some distinct redox peaks arise in the CV curves, indicating deeper redox reactions on the surface of both electrode materials. As expected, the charge–discharge curves of the HSCs at current density of 1 A g^{-1} are still nearly symmetric at an operating potential as high as 1.6 V (Fig. 6c), indicating that the device exhibits ideal capacitive characteristics with a rapid *I–V* response and low equivalent series resistance. In addition, there is no significant change in internal resistance (from *IR* drop) as shown in Fig. S6 (ESI†), which confirms the low equivalent series resistance of the HSCs. Fig. 6d shows the specific capacitance of the HSCs based on galvanostatic charge–discharge curves collected at 1 A g^{-1} as a function of the potential window. It is worth mentioning that the calculated specific capacitance significantly increased from 55 to 83 F g^{-1} when voltage windows were extended from 0.8 to 1.6 V. Accordingly, the energy density of the HSCs is also greatly improved from 5 to 29.35 W h kg^{-1}, an enhancement of more than 487%.

Fig. 7a presents CV curves of the HSCs at different sweep rates ranging from 10 to 100 mV s^{-1} between 0 and 1.6 V. Each curve exhibits symmetric and same shape without shape distortion, even at a high sweep rate, illustrating the desirable rapid charge/discharge property as a result of the effective electronic/ionic transmission of the electrode materials. To further evaluate the performance of the HSCs, we measured GCD curves at various current densities from 0.5 to 10 A g^{-1}, as shown in Fig. 7b. These linear shape discharge curves again confirm the excellent capacitive and good reaction reversibility of the HSCs, which is in congruent with CV analysis. The specific capacitances of the HSCs calculated based on the GCD curves are plotted as a function of the current density in Fig. 7C. The HSCs can deliver a high specific capacitance of 99 F g^{-1} at a current density of 0.5 A g^{-1}, and the capacitance retention is about 69% (68.3 F g^{-1}) with a twentyfold increase in the current density (Fig. 7c), indicating the sufficient redox reactions resulted from rapid ion diffusion even at high current densities. Meanwhile, the specific capacitance calculated based on the integral formula of CV curves also confirms the good kinetic performance. Based on the total mass of the active materials (Fig. 7a), the constructed HSC delivers a specific capacitance as high as 84.3 F g^{-1} at low sweep rate of 10 mV s^{-1}, and can still keep about 50% of original specific capacitance even at high sweep rate of 100 mV s^{-1}. To ascertain the durability for practical applications, the long-term cycling stability of the GR/VN//GN/V_2O_5 HSCs at a current density of 10 A g^{-1} is presented in Fig. 7d. Impressively, only 4.2% capacitance attenuation is observed during the early 3000 cycles, and it still keeps 90% of its original specific capacitance even after 7000 cycles. The morphologies of the electrode materials after cycling are given in Fig. S7 (ESI†). It can clearly see that there is no obvious change in the nanosphere morphology which is uniformly

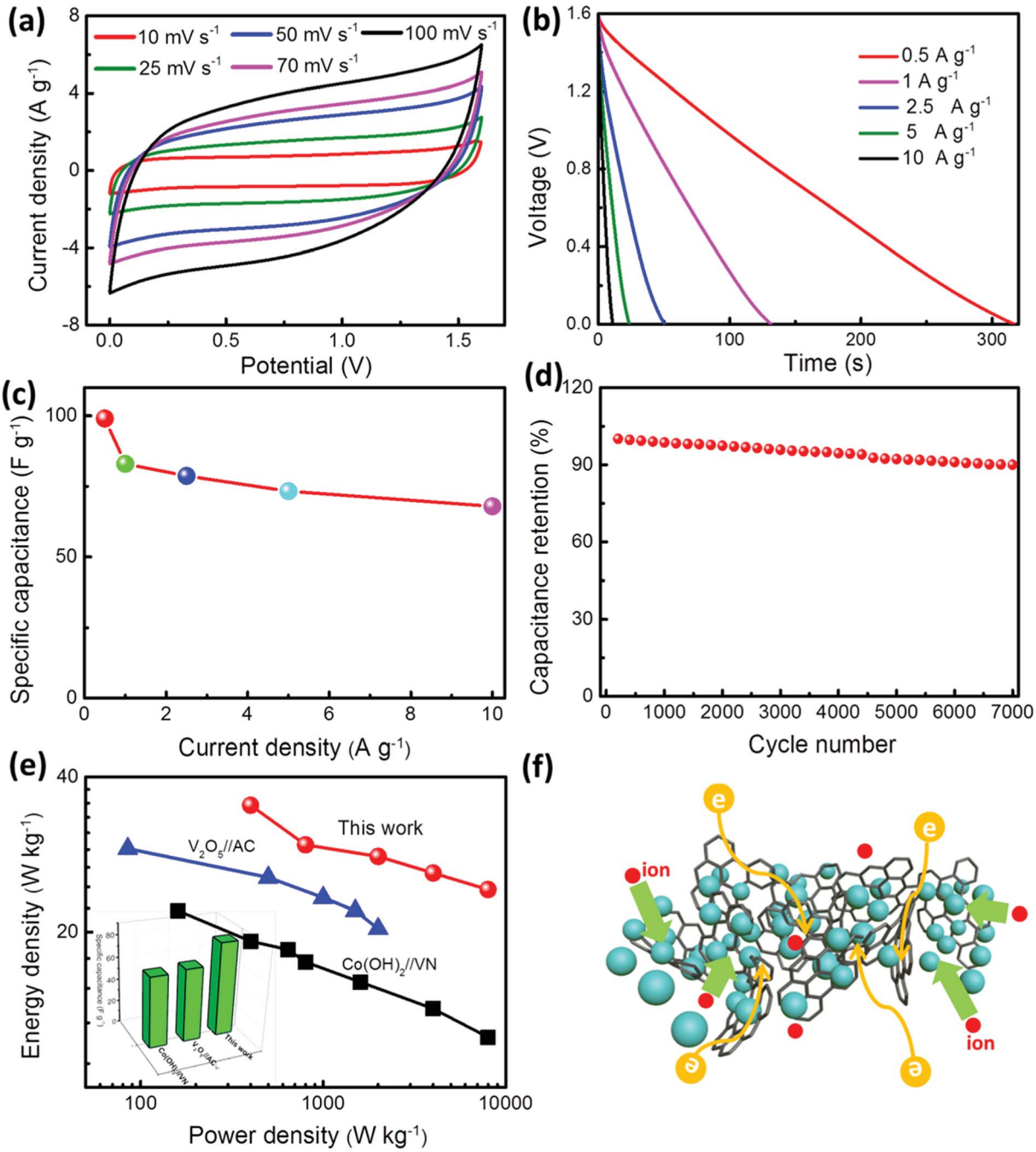

Fig. 7 (a) CV curves of the as-fabricated HSCs measured at different sweep rates from 0 to 1.6 V. (b) Galvanostatic discharge curves collected at different current densities. (c) Specific capacitance calculated from discharge curves as a function of the current density. (d) Cycling performance at a constant current density of 10 A g^{-1}. (e) Ragone plots of our HSCs in comparison with previously reported HSCs based on vanadium-based electrode materials with aqueous electrolyte (blue plots,[44] black plots,[16]), inset image is the corresponding specific capacitance of these HSCs calculated from discharge curves at current density of 1 A g^{-1}. (f) Schematic of intimate between the VN or V_2O_5 nanospheres and graphene facilitating rapid charge and electrolyte transport.

wrapped by crumpled graphene nanosheets after cycling. This result is mainly due to the good structural stability of our as-prepared electrode material. In addition, energy and power density are important parameters for evaluating the performance of energy-storage devices. The Ragone plots in Fig. 7e compare the performance of our HSCs to those of previously reported HSCs based on vanadium-based electrode materials with aqueous electrolyte. An energy density as high as 35.2 W h kg^{-1} can be achieved at a power density of 0.4 kW kg^{-1}, and an energy density of 24.15 W h kg^{-1} is maintained even at a high power density of 8 kW kg^{-1}. These values compare favorably to those of vanadium-based materials, such as the urchin-like VN (22 W h kg^{-1}, 0.16 kW kg^{-1}) and V_2O_5 nanoribbons (29 W h kg^{-1}, 0.085 kW kg^{-1}). The inset image in Fig. 7e

further compares the specific capacitance of the corresponding materials and the as-prepared HSCs represent the highest specific capacitance at the same current density (1 A g^{-1}). As concluded in Fig. 7f, the high performance of our HSCs is due to: (1) highly conductive GR wrapping on the surface of VN or V_2O_5 nanospheres, which not only enhances the electronic conductivity of the both electrodes but also suppresses electrochemical oxidation and dissolution of the VN; (2) the interpenetrating porous network structure consisting of intimately intertwined GR, which provides effective electron and electrolyte transport with more available active-sites; and (3) synergistic effect between pseudo-capacitive positive (GR/V_2O_5 NSP) and negative (GR/VN NSP) electrode materials with high specific capacitance values, which increases specific capacitance of the HSCs.

4. Conclusion

To conclude, based on a facile strategy, a graphene oxide (GO)-wrapped VO_x nanosphere (GO-wrapped VO_x NSP) precursor has been fabricated *via* a one-step solvothermal method, and through different thermal treatments it can be steadily transformed to GR/VN NSP and GR/V_2O_5 NSP, suitable for both electrodes in HSCs. The conformally wrapped GR has a significant influence on the electrochemical performance of VN and V_2O_5, derived from the simultaneous improvements in electronic conductivity, structural stability, and electrolyte transport. Benefitting from these merits, the as-prepared GR/VN NSP and GR/V_2O_5 NSP exhibit excellent electrochemical performance for HSCs with high specific capacitance (83 F g^{-1}) and good-long cycle life (90% specific capacitance retained after 7000 cycles). Furthermore, GR/VN NSP//GR/V_2O_5 NSP HSCs can deliver a high energy density of 35.2 W h kg^{-1} at 0.4 W kg^{-1} and maintains about 70% even at a high power density of 8 kW kg^{-1}. The facile strategy of fabricating negative and positive electrode materials derived from a single precursor can be extended to other functional materials for different integrated devices and the impressive results presented here show great potential in vanadium-based electrode materials for promising applications in the high performance energy storage systems.

Conflicts of interest

The authors declare no competing financial interest.

Acknowledgements

The authors acknowledge the support of the National Natural Science Foundation of China (Granted No. U1503292, No. 51472182), the Fundamental Research Funds for the Central Universities, and the National Key Research and Development Program of China (Granted No. 2017YFA0204600).

References

1 D. Larcher and J. M. Tarascon, *Nat. Chem.*, 2015, **7**, 19–29.
2 P. Simon, Y. Gogotsi and B. Dunn, *Science*, 2014, **343**, 1210–1211.
3 M. Zhi, C. Xiang, J. Li, M. Li and N. Wu, *Nanoscale*, 2013, **5**, 72–88.
4 G. Wang, L. Zhang and J. Zhang, *Chem. Soc. Rev.*, 2012, **41**, 797–828.
5 Y. Gogotsi and P. Simon, *Science*, 2011, **334**, 917–918.
6 L. Yu, B. Guan, W. Xiao and X. W. Lou, *Adv. Energy Mater.*, 2015, **5**, 1500981.
7 P. Simon and Y. Gogotsi, *Nat. Mater.*, 2008, **7**, 845–854.
8 D. P. Dubal, O. Ayyad, V. Ruiz and P. Gómez-Romero, *Chem. Soc. Rev.*, 2015, **44**, 1777–1790.
9 H. Xia, C. Hong, X. Shi, B. Li, G. Yuan, Q. Yao and J. Xie, *J. Mater. Chem. A*, 2015, **3**, 1216–1221.
10 N. Jabeen, A. Hussain, Q. Xia, S. Sun, J. Zhu and H. Xia, *Adv. Mater.*, 2017, **29**, 1700804.
11 G. Saeed, S. Kumar, N. H. Kim and J. H. Lee, *Chem. Eng. J.*, 2018, **352**, 268–276.
12 Y. Cheng, H. Zhang, S. Lu, C. V. Varanasi and J. Liu, *Nanoscale*, 2013, **5**, 1067–1073.
13 H. Kim, M. Y. Cho, M. H. Kim, K. Y. Park, H. Gwon, Y. Lee, K. C. Roh and K. Kang, *Adv. Energy Mater.*, 2013, **3**, 1500–1506.
14 L. Huang, B. Yao, J. Sun, X. Gao, J. Wu, J. Wan, T. Li, Z. Hu and J. Zhou, *J. Mater. Chem. A*, 2017, **5**, 2897–2903.
15 L. Wang, H. Yang, X. Liu, R. Zeng, M. Li, Y. Huang and X. Hu, *Angew. Chem.*, 2017, **129**, 1125–1130.
16 S. Kumar, G. Saeed, N. H. Kim and J. H. Lee, *J. Mater. Chem. A*, 2018, **6**, 7182–7193.
17 T. Zhai, X. Lu, Y. Ling, M. Yu, G. Wang, T. Liu, C. Liang, Y. Tong and Y. Li, *Adv. Mater.*, 2014, **26**, 5869–5875.
18 S. Sun, T. Zhai, C. Liang, S. V. Savilov and H. Xia, *Nano Energy*, 2018, **45**, 390–397.
19 S. S. Raut and B. R. Sankapal, *New J. Chem.*, 2016, **40**, 2619–2627.
20 R. Wang, X. Yan, J. Lang, Z. Zheng and P. Zhang, *J. Mater. Chem. A*, 2014, **2**, 12724–12732.
21 R. Wang, J. Lang, P. Zhang, Z. Lin and X. Yan, *Adv. Funct. Mater.*, 2015, **25**, 2270–2278.
22 Y. Yang, K. Shen, Y. Liu, Y. Tan, X. Zhao, J. Wu, X. Niu and F. Ran, *Nano-Micro Lett.*, 2017, **9**, 6.
23 J. Balamurugan, G. Karthikeyan, T. Thanh, N. Kim and J. Lee, *J. Power Sources*, 2016, **308**, 149–157.
24 X. Lu, M. Yu, T. Zhai, G. Wang, S. Xie, T. Liu, C. Liang, Y. Tong and Y. Li, *Nano Lett.*, 2013, **13**, 2628–2633.
25 C. M. Ghimbeu, E. Raymundo-Piñero, P. Fioux, F. Beguin and C. Vix-Guterl, *J. Mater. Chem.*, 2011, **21**, 13268–13275.
26 L. Zhang, C. Holt, E. Luber, B. Olsen, H. Wang, M. Danaie, X. Cui, X. Tan, V. Lui, W. Kalisvaart and D. Mitlin, *J. Phys. Chem. C*, 2011, **115**, 24381–24393.
27 Q. Zhang, X. Wang, Z. Pan, J. Sun, J. Zhao, J. Zhang, C. Zhang, L. Tang, J. Luo, B. Song, Z. Zhang, W. Lu, Q. Li, Y. Zhang and Y. Yao, *Nano Lett.*, 2017, **17**, 2719–2726.
28 B. Yan, X. Li, Z. Bai, Y. Zhao, L. Dong, X. Song, D. Li, C. Langford and X. Sun, *Nano Energy*, 2006, **24**, 32–44.
29 Y. Wu, G. Gao, H. Yang, W. Bi, X. Liang, Y. Zhang, G. Zhang and G. Wu, *J. Mater. Chem. A*, 2015, **3**, 15692–15699.

30 W. Sun, A. Du, B. Zhou, J. Shen, S. Huang and J. Tang, *J. Sol-Gel Sci. Technol.*, 2016, **80**, 68–76.
31 W. Sun, A. Du, G. Gao, J. Shen and G. Wu, *Microporous Mesoporous Mater.*, 2017, **253**, 71–79.
32 Y. Wu, G. Gao and G. Wu, *J. Mater. Chem. A*, 2015, **3**, 1828–1832.
33 X. Xiao, X. Peng, H. Jin, T. Li, C. Zhang, B. Gao, B. Hu, K. Huo and J. Zhou, *Adv. Mater.*, 2013, **25**, 5091–5097.
34 M. Cakici, R. R. Kakarla and F. Alonso-Marroquin, *Chem. Eng. J.*, 2017, **309**, 151–158.
35 V. Augustyn, J. Come, M. A. Lowe, J. Kim, P. L. Taberna, S. H. Tolbert, H. D. Abruna, P. Simon and B. Dunn, *Nat. Mater.*, 2013, **12**, 518–522.
36 A. Jayakumar, R. P. Antony, R. Wang and J. M. Lee, *Small*, 2017, **13**, 1603102.
37 T. Brousse, D. Bélanger and J. W. Long, *J. Electrochem. Soc.*, 2015, **162**, A5185–A5189.
38 B. Li, F. Dai, Q. Xiao, L. Yang, J. Shen, C. Zhang and M. Cai, *Energy Environ. Sci.*, 2016, **9**, 102–106.
39 G. Godillot, P. L. Taberna, B. Daffos, P. Simon, C. Delmas and L. Guerlou-Demourgues, *J. Power Sources*, 2016, **331**, 277–284.
40 W. Jiang, D. Yu, Q. Zhang, K. Goh, L. Wei, Y. Yong, R. Jiang, J. Wei and Y. Chen, *Adv. Funct. Mater.*, 2015, **25**, 1063–1073.
41 A. M. Glushenkov, D. Hulicova-Jurcakova, D. Llewellyn, G. Q. Lu and Y. Chen, *Chem. Mater.*, 2010, **22**, 914–921.
42 D. Choi, G. E. Blomgren and P. N. Kumta, *Adv. Mater.*, 2006, **18**, 1178–1182.
43 M. Li, G. Sun, P. Yin, C. Ruan and K. Ai, *ACS Appl. Mater. Interfaces*, 2013, **5**, 11462–11470.
44 Q. T. Qu, Y. Shi, L. L. Li, W. L. Guo, Y. P. Wu, H. P. Zhang, S. Y. Guan and R. Holze, *Electrochem. Commun.*, 2009, **11**, 1325–1328.